



Andres, S., Steinmann, P. and Budday, S. (2018) The origin of compression influences geometric instabilities in bilayers. *Proceedings of the Royal Society of London Series A: Mathematical, Physical and Engineering Sciences*, 474(2217), 20180267.

There may be differences between this version and the published version. You are advised to consult the publisher's version if you wish to cite from it.

<http://eprints.gla.ac.uk/169384/>

Deposited on: 8 October 2018

Enlighten – Research publications by members of the University of Glasgow\_  
<http://eprints.gla.ac.uk>



**Subject Areas:**

Mechanics, Biomechanics,  
Mechanical Engineering

**Keywords:**

Thin films, Bilayered systems,  
Instabilities, Post-wrinkling,  
Bifurcations, Soft matter

**Author for correspondence:**

Silvia Budday

e-mail: [silvia.budday@fau.de](mailto:silvia.budday@fau.de)

# The origin of compression influences geometric instabilities in bilayers

Sebastian Andres<sup>1</sup>, Paul Steinmann<sup>1,2</sup>,  
and Silvia Budday<sup>1</sup>

<sup>1</sup>Chair of Applied Mechanics, University of  
Erlangen-Nürnberg, Germany

<sup>2</sup>Glasgow Computational Engineering Centre, UK

Geometric instabilities in bilayered structures control the surface morphology in a wide range of biological and technical systems. Depending on the application, different mechanisms induce compressive stresses in the bilayer. However, the impact of the chosen origin of compression on the critical conditions, post-buckling evolution and higher-order pattern selection remains insufficiently understood. Here, we conduct a numerical study on a finite element setup and systematically vary well-known factors contributing to pattern selection under the four main origins of compression: film growth, substrate shrinkage and whole-domain compression with and without pre-stretch. We find that the origin of compression determines the substrate stretch state at the primary instability point and thus significantly affects the critical buckling conditions. Similarly, it leads to different post-buckling evolutions and secondary instability patterns when the load further increases. Our results emphasize that future phase diagrams of geometric instabilities should incorporate not only the film thickness but also the origin of compression. Thoroughly understanding the influence of the origin of compression on geometric instabilities is crucial to solve real-life problems such as the engineering of smart surfaces or the diagnosis of neuronal disorders, which typically involve temporally or spatially combined origins of compression.

## 1. Introduction

In recent years, geometric instabilities in bilayered structures have been extensively studied with regard to wrinkling phenomena in both biological and technical systems. Well known examples in biology are the wrinkling of the skin of humans, animals and plants [1,2], the wrinkling of biofilms [3], the large inward folds observed in airways of patients suffering from asthma or chronic bronchitis [4,5], and the convoluted surface morphology of mammalian cerebral cortices [6–10]. Abnormal folding patterns in human brains, for instance, are associated with severe neurological disorders such as autism and schizophrenia [11,12]. Technical applications involve manufacturing of stretchable electronic components [13], electronic skin [14] and pressure-sensitive diffraction gratings [15] used to measure the Young's moduli of thin polymeric films and coatings [16].

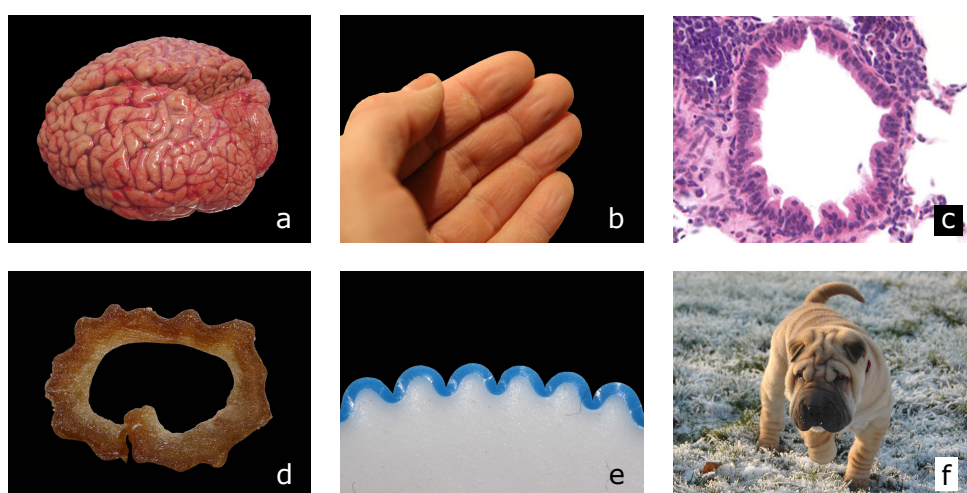


**Figure 1.** Examples of geometric instabilities in layered systems: (a) convolutions of the mammalian cerebral cortex, (b) wrinkling of fingertips immersed in water, (c) folding in asthmatic airways, adapted from [17] under Creative Commons Attribution License, (d) wrinkled skin of a dried date, (e) folding of a PDMS film on a pre-stretched PDMS substrate, photography of samples previously published in [18], (f) folded skin of Shar Pei whelps, adapted under Creative Commons CC0.

In all the above mentioned applications, the occurrence of geometric instabilities originates from film compression. However, depending on the application, two different mechanisms underlie the emergence of compressive stresses in the film (see Figure 2). The first is driven by differential growth or expansion of film and substrate: the film has to grow/expand faster than the substrate. For instance, recent evidence suggests that the surface morphology of mammalian cerebral cortices evolves as the outer layers of the brain grow faster than the core during embryonic development [10]. Likewise, substrate shrinkage (= negative growth/expansion) can induce instabilities: In [19], for instance, a thermally expanded PDMS (polydimethylsiloxane) substrate is coated with a thin metallic film, which – upon cooling – exhibits wrinkling patterns. In this case the substrate shrinks faster than the film as the coefficient of thermal expansion of polymers is generally much larger than that of metals. The second mechanism is based on a whole domain compression of bilayers, which is often used in experimental setups. It can be achieved by bending a bilayer [20] or by imposing transversal contraction [16]. Alternatively, the substrate can be stretched prior to attaching the film with a subsequent relaxation of the bilayer [18,20,21]. It is important to note that for nonlinear materials pre-stretching the substrate will affect the stiffness ratio between film and substrate and will thus affect the critical compression and resulting surface

morphology [22]. Interestingly, a recent study proves that buckling instabilities can also occur in tension, namely for layered structures with frictionless and bilateral interfaces [23]. However, in the current work we will limit ourselves to the more common phenomenon of buckling under compression.

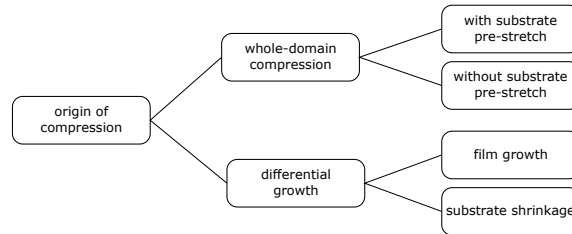


**Figure 2.** Overview over the different mechanisms to invoke film compression in bilayers. Although the origins of compression are compared individually in this work, combinations are possible.

Previous parameter studies on the critical conditions and post-buckling morphology of geometric instabilities have mainly focused on the influence of the film thickness, the stiffness ratio and the adhesion energy between the layers [21]. Additionally, the impact of substrate pre-stretch has been studied in computational setups based on a whole-domain compression of the bilayer [22]. However, a comparative evaluation of the critical conditions for primary wrinkling and the highly nonlinear post-buckling evolution for different origins of compression is still in need. Holland et al. [24] studied different origins of compression using a semi-analytical linear perturbation analysis, which is limited to stiffness ratios close to unity, very small substrate pre-stretches and infinitesimal deformations past the instability point. In this work, we conduct a numerical study which aims to overcome the inherent limitations of analytical approaches. We compare the four main origins of compression on the same reference setup: film growth, substrate shrinkage and whole-domain compression with and without substrate pre-stretch. To this end, we evaluate the critical wavelength, the critical compression and the post-buckling evolution including secondary instabilities.

## 2. Analytical predictions

As classical analytical approaches studying instabilities in bilayered structures [25,26] aimed for closed-form solutions, they exhibit distinct limitations. These limitations include that only infinitesimal strains past the instability point and high stiffness ratios between film and substrate are admissible. Moreover, those approaches neglect all shear stresses between film and substrate. Consequently, the classical analytical analyses are not capable of differing between different origins of compression. Recent semi-analytical approaches (= analytical approaches without a closed-form solution, which consequently have to be solved numerically) presented in [22] and [24] account for shear stresses and the origin of compression. Still, they fail to describe the highly nonlinear post-buckling behavior of complex problems as they remain restricted to certain ranges in stiffness ratio, small post-buckling strains and simplified geometries. Nonetheless, analytical solutions provide valuable insight into qualitative effects of isolated parameters on the critical conditions and post-buckling morphology. Thus, we use a closed-form analytical solution presented in [27] accounting for substrate pre-stretch to obtain analytical estimates for the critical wavelength  $\lambda^c$  and critical film compression  $\delta^c$  of the examples studied. We consider a compressible, linear elastic plate bonded to an incompressible neo-Hookean substrate which has been stretched prior to film attachment. The bilayer undergoes a whole domain compression



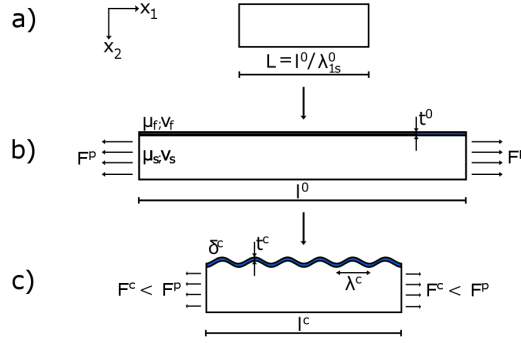


**Figure 3.** Analytical model problem: Whole-domain compression with pre-stretch. Substrate of initial length  $L = l^0 / \lambda_{1s}^0$  (a) is stretched to the length  $l^0$  through the force  $F^p$  and combined with a film of length  $l^0$  to form a pre-stretched bilayer. The substrate pre-stretch is then released (which is equivalent to a whole-domain compression) until the film of the bilayer wrinkles at a critical film compression  $\delta^c$  with the remaining force  $F^c < F^p$  (c). It is important to note, that the substrate generally is not stress-free at  $\delta^c$  and that the amplitude of the wrinkling pattern at the critical compression is still approximately zero, unlike in (c) depicted for illustrative purposes.

in plane strain (see Figure 3). This analytical model proved to provide sound predictions for stiffness ratios  $\mu_f / \mu_s > 10$ , where  $\mu$  denotes the classical shear modulus [22]. Indices f and s refer to quantities related to film and substrate, superscripts c and 0 refer to quantities at the instability point and in the undeformed configuration.

The substrate is pre-stretched with stretches  $(\lambda_{1s}^0, \lambda_{2s}^0, \lambda_{3s}^0)$ . Assuming incompressibility we obtain

$$\lambda_{1s}^0 \lambda_{2s}^0 \lambda_{3s}^0 = 1. \quad (2.1)$$

For a pre-stretch  $\lambda_{1s}^0$  in plane strain, Equation 2.1 yields

$$\lambda_{2s}^0 = \frac{1}{\lambda_{1s}^0}, \quad \lambda_{3s}^0 = 1. \quad (2.2)$$

Then the critical compression  $\delta^c = 1 - l^c / l^0$  of the bilayer and the associated critical wavelength  $\lambda^c$  can be calculated from

$$\delta^c = \frac{1}{4} \left[ 6\Lambda [1 - \nu_f] \frac{\mu_s}{\mu_f} \right]^{\frac{2}{3}} \quad \text{and} \quad \lambda^c = 2\pi t^c \left[ 6\Lambda [1 - \nu_f] \frac{\mu_s}{\mu_f} \right]^{-\frac{1}{3}}, \quad (2.3)$$

with  $\Lambda = \frac{1}{2} [1 + \lambda_{1s}^0]$  [27]. We denote the film thickness at the instability point by  $t^c$  and parametrize the film compressibility in terms of its Poisson's ratio  $\nu_f$ . In the absence of pre-stretch (i.e.  $\lambda_{1s}^0 = 1$ ) Equation 2.3 reduces to the classical Allen solution [26]. It is important to note that the analytical solution presented above is limited to infinitesimal post-buckling strains.

### 3. Computational model for different origins of compression

In this work, we propose a computational model capable of imposing the four main origins of compression simultaneously. Each origin is switched on and off by choosing the appropriate kinetic parameters. We define a total of 6 governing equations: the kinematics, the balance equation, the constitutive law, growth kinematics, growth kinetics, and dynamic Dirichlet boundary conditions enforcing whole-domain compression. We solve the highly nonlinear equations using the finite element method in a custom-designed environment implemented in MATLAB Release 2014a, The MathWorks, Inc., Natick, Massachusetts, USA. Although the chosen

reference problem could be solved in 2D, we chose a 3D formulation to ensure the applicability to real-life, three-dimensional problems.

### (a) Kinematics, Piola stress, balance equation

We introduce the deformation via the deformation gradient  $\mathbf{F}$  and its Jacobian  $J$ , which we decompose multiplicatively into an elastic and a growth contribution to accommodate for growth or shrinkage [28]

$$\mathbf{F} = \mathbf{F}^e \cdot \mathbf{F}^g \quad \text{and} \quad J = \det(\mathbf{F}) = J^e J^g. \quad (3.1)$$

Following standard arguments of thermodynamics, we derive the Piola stress  $\mathbf{P}$

$$\mathbf{P} = \frac{\partial \psi(\mathbf{F}^e)}{\partial \mathbf{F}} = \frac{\partial \psi(\mathbf{F}^e)}{\partial \mathbf{F}^e} : \frac{\partial \mathbf{F}^e}{\partial \mathbf{F}} = \mathbf{P}^e \cdot [\mathbf{F}^g]^{-t} \quad (3.2)$$

as the classical elastic Piola stress  $\mathbf{P}^e$  weighted by the growth deformation gradient  $\mathbf{F}^g$ . The Piola stress then enters the balance equation for mechanical equilibrium. In the absence of volume forces, it reduces to

$$\text{div}(\mathbf{P}) \doteq \mathbf{0}. \quad (3.3)$$

### (b) Constitutive equation

We define the constitutive law of a hyperelastic material in terms of its strain-energy density  $\psi$ , which only depends on the elastic part of the deformation gradient  $\mathbf{F}^e$ . We implement a neo-Hookean material model by its strain energy function

$$\psi(\mathbf{F}^e) = \frac{1}{2} \mu [\mathbf{F}^e : \mathbf{F}^e - 3 - 2 \ln(J^e)] + \frac{1}{2} \lambda \ln^2(J^e), \quad (3.4)$$

with the Lamé constants  $\mu$  and  $\lambda$ . We obtain the explicit expression for the elastic Piola stress  $\mathbf{P}^e$  as

$$\mathbf{P}^e = \frac{\partial \psi(\mathbf{F}^e)}{\partial \mathbf{F}^e} = \mu \mathbf{F}^e + [\lambda \ln(J^e) - \mu] [\mathbf{F}^e]^{-t}. \quad (3.5)$$

### (c) Growth kinematics and growth kinetics

We choose uniaxial growth as growth kinematics to mimic the polymer experiments in [18], which are based on uniaxially pre-stretched bilayers. Consequently, the growth part of the deformation gradient  $\mathbf{F}^g$  and its Jacobian can be expressed as

$$\mathbf{F}^g = \mathbf{I} + [\vartheta - 1] \mathbf{n} \otimes \mathbf{n} \quad \text{and} \quad J^g = \det(\mathbf{F}^g) = \vartheta, \quad (3.6)$$

where  $\mathbf{I}$  is the second order unit tensor and  $\mathbf{n}$  is the direction of growth/shrinkage. We define the growth multiplier  $\vartheta$  analogously to stretch as  $\vartheta = l_1/l_0$ , which corresponds to the relative change in length in the growth direction. By rephrasing Equation 3.1 we obtain the elastic part of the deformation gradient  $\mathbf{F}^e$  and its Jacobian  $J^e$ ,

$$\mathbf{F}^e = \mathbf{F} \cdot \mathbf{F}^{-g} = \mathbf{F} \cdot \left[ \mathbf{I} + \left[ \frac{1}{\vartheta} - 1 \right] \mathbf{n} \otimes \mathbf{n} \right] \quad \text{and} \quad J^e = \frac{\det(\mathbf{F})}{\det(\mathbf{F}^g)} = \frac{1}{\vartheta} J. \quad (3.7)$$

To describe the growth kinetics, we introduce constant growth rates  $G_f$  and  $G_s$  for the film and the substrate. We obtain the individual growth multipliers in the film and substrate by the integration of

$$\dot{\vartheta} = G_f \quad \text{and} \quad \dot{\vartheta} = G_s. \quad (3.8)$$

Depending on the choice of the growth rates  $G_f$  and  $G_s$  the film and substrate can grow, shrink or behave purely elastic. Table 1 provides an overview of  $\vartheta$ ,  $\mathbf{F}^g$ ,  $\mathbf{F}^e$  and  $\mathbf{P}$  for different growth kinetics.

$G$	growth $> 0$	shrinkage $< 0$	no growth / purely elastic $= 0$
$\vartheta$	$> 1$	$< 1$	$= 1$
$\mathbf{F}^g$	$\mathbf{I} + [\vartheta - 1]\mathbf{n} \otimes \mathbf{n}$	$\mathbf{I} + [\vartheta - 1]\mathbf{n} \otimes \mathbf{n}$	$\mathbf{I}$
$\mathbf{F}^e$	$\mathbf{F} \cdot [\mathbf{I} + [\frac{1}{\vartheta} - 1]\mathbf{n} \otimes \mathbf{n}]$	$\mathbf{F} \cdot [\mathbf{I} + [\frac{1}{\vartheta} - 1]\mathbf{n} \otimes \mathbf{n}]$	$\mathbf{F}$
$\mathbf{P}$	$\mathbf{P}^e \cdot [\mathbf{F}^g]^{-t}$	$\mathbf{P}^e \cdot [\mathbf{F}^g]^{-t}$	$\mathbf{P}^e$

**Table 1.** Growth and shrinkage in film and substrate are controlled solely via the growth rate  $G$ . Depending on the choice of  $G$ , the material either exhibits growth, shrinkage or behaves purely elastic.

In case of whole-domain compression, we prescribe time-dependent displacements  $u_x$  before entering the equation solver. We define the displacements by

$$\dot{u}_x = G_r l^0, \quad (3.9)$$

where  $G_r$  denotes the displacement rate and  $l^0$  is the initial film length.

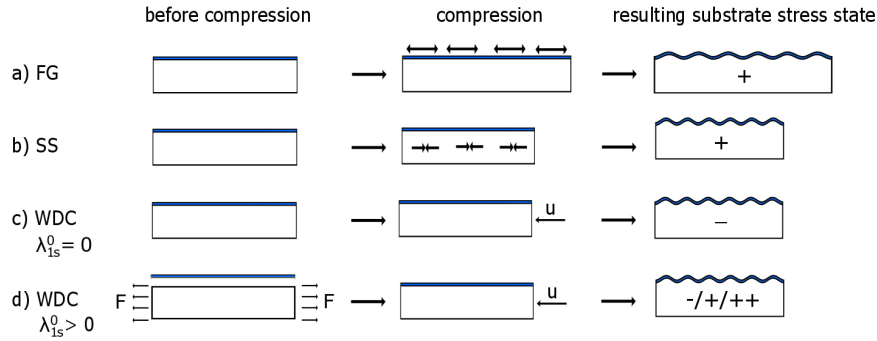


**Figure 4.** The four main origins of compression and the resulting substrate stress state: (a) film growth: the film grows while the substrate behaves purely elastic. As the domain is allowed to expand freely, the substrate is under modest tension at the instability point, (b) substrate shrinkage: the substrate shrinks while the film behaves purely elastic. As the domain is allowed to contract freely, the substrate is under modest tension at the instability point, (c) whole-domain compression: film and substrate behave purely elastic, the whole bilayer is compressed by a prescribed displacement and therefore under compressive stress, (d) whole-domain compression with substrate pre-stretch: substrate is stretched prior to whole-domain compression. Depending on the magnitude of the pre-stretch, the substrate can be under compression, modest tension or large tension.

## (d) Numerics

We employ the finite element method to discretize the problem and solve the governing equations at each time step with a standard Newton-Raphson iteration scheme. First, the growth multiplier

of the film  $\vartheta_f$  and the substrate  $\vartheta_s$  and the prescribed displacement  $u_x$  are updated by an explicit Euler integration scheme, yielding

$$\vartheta_f^{n+1} = \vartheta_f^n + \Delta\tau G_f, \quad \vartheta_s^{n+1} = \vartheta_s^n + \Delta\tau G_s, \quad u_x^{n+1} = u_x^n + \Delta\tau G_r l^0, \quad (3.10)$$

where  $\Delta\tau$  denotes the time step increment. Once the growth multiplier  $\vartheta$  at a given time step is fixed, the Piola stress  $\mathbf{P}$  and its corresponding tangent modulus  $\mathbf{A}$  are computed and enter the Newton-Raphson iteration. We compute the tangent modulus  $\mathbf{A}$  as the total derivative of  $\mathbf{P}$  with respect to  $\mathbf{F}$ . For the neo-Hookean material model this yields

$$\begin{aligned} \mathbf{A} &= \frac{d\mathbf{P}}{d\mathbf{F}} = \left. \frac{\partial \mathbf{P}}{\partial \mathbf{F}} \right|_{\vartheta} = \\ &= \mu \mathbf{I} \otimes \mathbf{I} \cdot [\mathbf{F}^{-g} \cdot [\mathbf{F}^g]^{-t}] + [\mu - \lambda \ln(\frac{J}{\vartheta^2})] \mathbf{F}^{-t} \otimes \mathbf{F}^{-1} + \lambda \mathbf{F}^{-t} \otimes \mathbf{F}^{-t}. \end{aligned} \quad (3.11)$$

We abbreviated non-standard fourth order tensor products to  $\{\bullet \otimes \circ\}_{ijkl} = \{\bullet\}_{ik} \{\circ\}_{jl}$  and  $\{\bullet \otimes \circ\}_{ijkl} = \{\bullet\}_{il} \{\circ\}_{jk}$  to shorten notation.

### (e) Reference problem

For the comparative evaluation of different origins of compression, we chose the reference problem of a rectangular bilayer in plane strain. It is the most commonly used problem in analytical [9,22,24–27] and numerical approaches [21,22,29–33] towards geometric instabilities in bilayered structures. While experimental designs are necessarily conducted in plane stress, conclusions from plane strain models have proven applicable to plane stress as well [14,15,18,20,21,27,34]. All surfaces except the right edge and the top of the bilayer are confined to tangential displacement. While the top surface remains unconfined, we couple the x-displacements of all nodes on the right face to enforce that it remains vertical (see Figure 5). It is either allowed to move freely along the x-axis (film growth, substrate shrinkage) or a displacement is prescribed (whole-domain compression with/without pre-stretch).

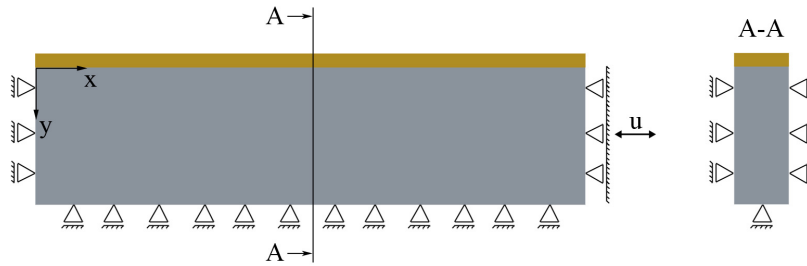


**Figure 5.** Geometry and boundary conditions of the reference problem for comparing different origins of compression. Displacement  $u$  of the right hand side boundary can either be an unknown or prescribed.

We chose an identical material model for all origins of compression and calibrated the corresponding parameters using the stress-strain curves according to experiments on PDMS bilayers in [18]. We obtained the material parameters from uniaxial tensile tests on a custom-built tensile testing device (Hegewald & Peschke) with samples according to DIN 53504 Type S3. For the film, we determined the Lamé constants as  $\mu = 2.233 \text{ N/mm}^2$  and  $\lambda = 20.093 \text{ N/mm}^2$ . For the substrate, we found  $\mu = 0.077 \text{ N/mm}^2$  and  $\lambda = 0.690 \text{ N/mm}^2$ . These material constants

correspond to slight compressibility at  $\nu = 0.45$ .

### (f) Perturbation

Our reference problem does not feature geometrical imperfections or gradients in material stiffness, thus a perturbation is necessary to avoid overly high buckling strains [35]. We introduce the perturbation in the center of the geometric domain by prescribing a slight uniaxial shrinkage perpendicular to the film in a vertical band of substrate elements during the first few time steps. It is important to note, that the perturbation is non-periodic and therefore does not predetermine the critical wavelength of the buckling pattern [35]. Width and magnitude of the perturbation were chosen small enough that neither the critical wavelength nor the critical film compression was affected by the perturbation. This was ensured through an extensive sensitivity analysis.

### (g) Meshing

The rectangular bilayer is discretized with a very dense mesh of 1 element per 0.5mm in x-/y-/z-direction and 5 Elements across the film thickness. We chose tri-quadratic Lagrangian 27-node hexahedral elements for being resilient to locking effects in problems involving geometric instabilities [31]. As we aim to *quantitatively* compare different origins of compression, we conducted a numerical study beforehand to ensure the adequacy of the chosen discretization. The numerical discretization error proved negligible for critical wavelengths  $\lambda^c \geq 3\text{mm}$  (i.e. 6 elements per wavelength). Below this threshold, the film behaves overly stiff and thus critical compression  $\delta^c$  and critical wavelength  $\lambda^c$  exhibit unrealistically large values.

## 4. Results

The main factors contributing to pattern selection in buckling instabilities are the critical film thickness  $t^c$ , the stiffness ratio  $\mu_f/\mu_s$  and, for the case of whole-domain compression, the pre-stretch  $\lambda_{1s}^0$ . In the following, we systematically vary all three factors to assess the influence of the origin of compression on the buckling behavior. We performed 9 numerical series to investigate primary wrinkling: two series per origin of compression (see Figure 2), in which we varied the film thickness (10 steps,  $t^0 \in [0.15\text{mm}; 0.60\text{mm}]$ ) and the stiffness ratio (10 steps,  $\mu_f/\mu_s \in [5; 150]$ ) and a numerical series in which we varied the pre-stretch (15 steps,  $\lambda_{1s}^0 \in [1; 5]$ ). Additionally, we performed 10 numerical series to investigate secondary pattern selection: six series in which we vary the stiffness ratio  $\mu_f/\mu_s$  (10 steps,  $\mu_f/\mu_s \in [5; 150]$ ) at pre-stretches  $\lambda_{1s}^0 = 1.0, 1.5, 1.75, 2.0, 2.5, 3.0$  and four series in which we vary the pre-stretch (10 steps,  $\lambda_{1s}^0 \in [1; 3]$ ) at stiffness ratios  $\mu_f/\mu_s = 5, 10, 30, 70$ .

### (a) Primary wrinkling instability

Once the gradually increasing compression in the film reaches a critical value, the system becomes unstable and the initially flat film wrinkles (this only holds for stiffness ratios considerably larger than unity). For a comprehensive comparison of different origins of compression, we evaluated the main characteristics of primary wrinkling instabilities: the critical wavelength  $\lambda^c$  and the critical film compression  $\delta^c$ .

#### (i) Critical wavelength

Figure 6 plots the critical wavelength  $\lambda^c$  as a function of the critical film thickness  $t^c$ . The linear relation predicted by the analytical solution in Section 2 is apparent regardless of the origin of compression. We observe that film growth and substrate shrinkage yield almost identical wavelengths. For whole-domain compression without pre-stretch, we obtain slightly longer wavelengths than for differential growth, while whole-domain compression with pre-stretch

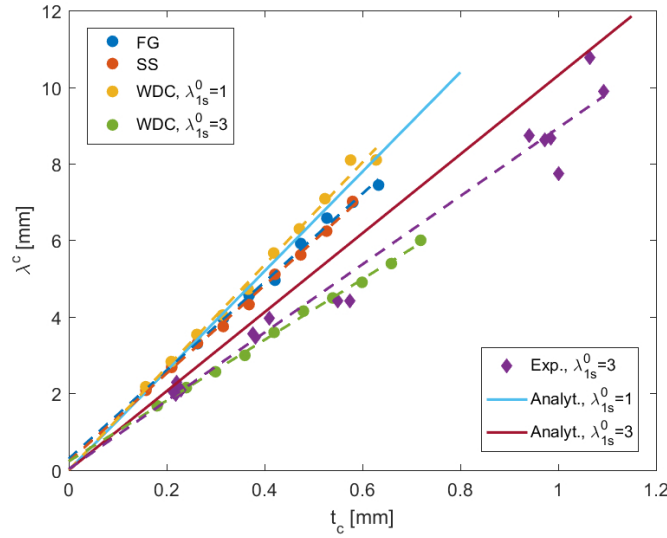
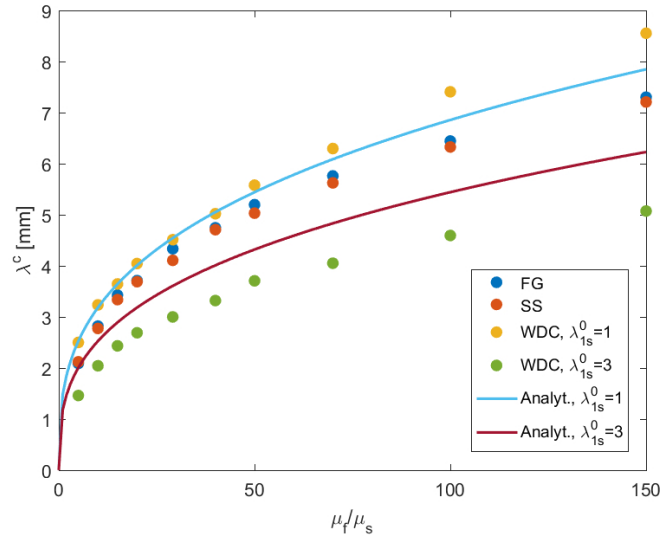


**Figure 6.** Critical wavelength  $\lambda^c$  as a function of the critical film thickness  $t^c$  for stiffness ratio  $\mu_f/\mu_s = 29$ . The computational results for film growth (FG), substrate shrinkage (SS) and whole-domain compression (WDC) at substrate pre-stretches  $\lambda_{1s}^0 = 1$  and  $\lambda_{1s}^0 = 3$  are compared to the analytical solution [27] and experimental results previously published in [18]. Corresponding linear regressions are depicted as dashed lines.

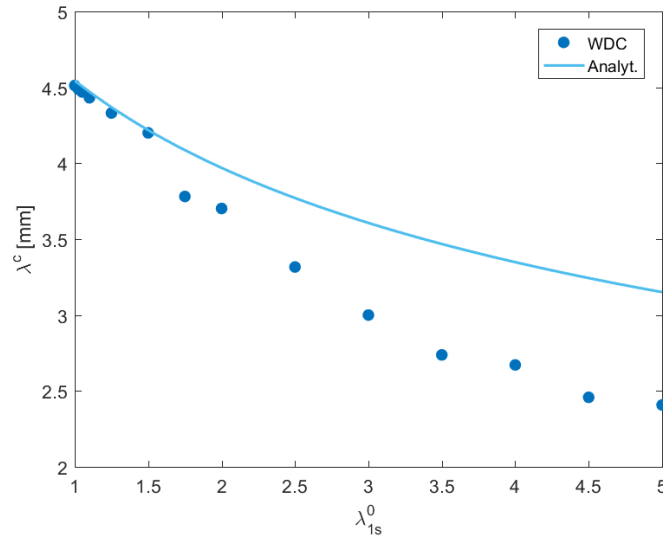
$\lambda_{1s}^0 = 3$  yields significantly shorter wavelengths. We attribute this observation to differences in substrate stretch at the instability point: for whole-domain compression with pre-stretch the substrate is under tension ( $\lambda_{1s}^c = 2.70$ ), while in the absence of pre-stretch the substrate is under compression ( $\lambda_{1s}^c = 0.94$ ). Due to the nonlinear stress-strain relation of the neo-Hookean material model, a stretched substrate affects the stiffness ratio  $\mu_f/\mu_s$  at the instability point and therefore the critical wavelength  $\lambda^c$ . This rationale seems consistent when we compare whole-domain compression without pre-stretch to differential growth and the analytical solution assuming  $\lambda_{1s}^0 = 1$ . For the case of differential growth, the substrate is under modest tension at the instability point ( $\lambda_{1s}^c = 1.027 - 1.116$ , depending on  $t^0$ ), which accounts for slightly shorter critical wavelengths  $\lambda^c$ . In the analytical solution, the substrate is assumed to be in a strain-free state and consequently the predicted critical wavelengths  $\lambda^c$  are between those obtained for whole-domain compression and differential growth. In Figure 6 we further included experimental data for whole-domain compression with a substrate pre-stretch  $\lambda_{1s}^0 = 3$ , previously published in [18]. Interestingly, while experimental and numerical results agree well, the analytical solution fails to predict the numerical results for large substrate pre-stretch. We will revisit this issue when discussing Figure 8, which illustrates the wrinkling wavelength as a function of the substrate pre-stretch.

Figure 7 plots the critical wavelength  $\lambda^c$  as a function of the stiffness ratio  $\mu_f/\mu_s$ . Analytical approaches predict the critical wavelength  $\lambda^c$  to be proportional to the cubic root of the stiffness ratio  $\mu_f/\mu_s$ . The numerical data seem to support this prediction regardless of the origin of compression. Furthermore, the graph confirms the conclusions drawn from Figure 6: film growth and substrate shrinkage yield virtually identical wavelengths, while substrate pre-stretch will lead to smaller wavelengths. Again, the analytical solution for  $\lambda_{1s}^c = \lambda_{1s}^0 = 1$  is nested between the results for whole-domain compression without pre-stretch ( $\lambda_{1s}^c < 1$ ) and deviates significantly from the numerical results for large substrate pre-stretch.

Figure 8 illustrates the effect of substrate pre-stretch varied between  $\lambda_{1s}^0 = 1$  (no pre-stretch) and  $\lambda_{1s}^0 = 5$  (large pre-stretch) on the critical wavelength  $\lambda^c$ . Increasing pre-stretch  $\lambda_{1s}^0$  correlates



**Figure 7.** Critical wavelength  $\lambda^c$  as a function of the stiffness ratio  $\mu_f/\mu_s$  for film growth (FG), substrate shrinkage (SS) and whole-domain compression (WDC) at substrate pre-stretches  $\lambda_{1s}^0 = 1$  and  $\lambda_{1s}^0 = 3$ . The computational results are compared to the analytical solution in [27]. All results correspond to a critical film thickness of  $t^c = 0.35\text{mm}$ .



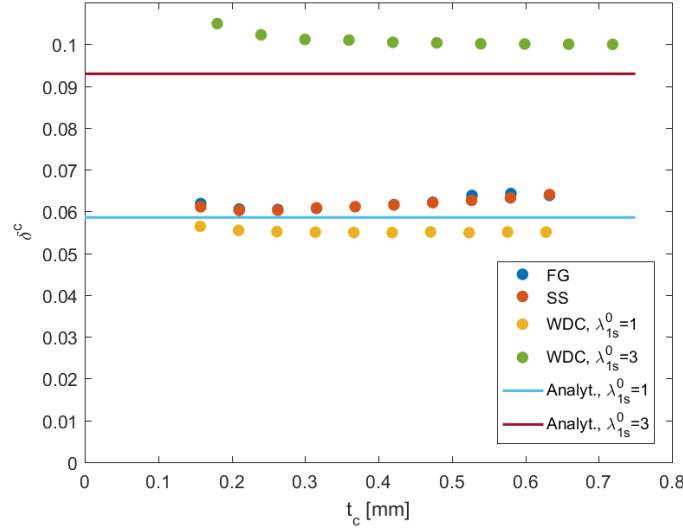
**Figure 8.** Critical wavelength  $\lambda^c$  as a function of the stiffness ratio substrate pre-stretch  $\lambda_{1s}^0$  for stiffness ratio  $\mu_f/\mu_s = 29$  and critical film thickness  $t^c = 0.35\text{mm}$ . Computational results for whole-domain compression (WDC) are compared to the analytical solution in [27].

with decreasing critical wavelengths  $\lambda^c$ . Interestingly, the numerical results deviate from the analytical solution for pre-stretches  $\lambda_{1s}^0 > 1.5$ . We can rule out that the deviation of numerical and analytical results is caused by discretization errors, as an insufficient discretization typically causes larger rather than shorter critical wavelengths  $\lambda^c$ . We conclude that Figure 8 reveals the symptomatic restriction of analytical approaches to small strains. This limitation also explains



why the analytical and numerical results disagree for large pre-stretches  $\lambda_{1s}^0 = 3$  in Figures 6 and 7. Our results indicate, that the analytical solution is only applicable to pre-stretches below a threshold of  $\lambda_{1s}^0 \approx 1.5$ .

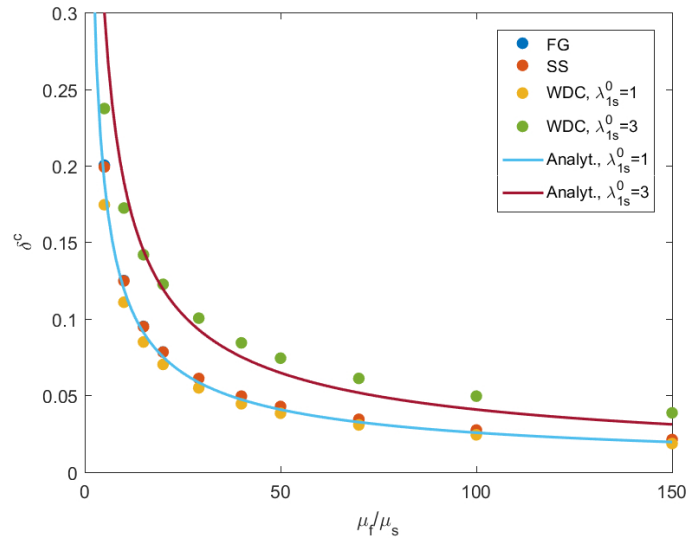
## (ii) Critical compression



**Figure 9.** Critical compression  $\delta^c$  as a function of the critical film thickness  $t^c$  for stiffness ratio  $\mu_f/\mu_s = 29$ . The computational results for film growth (FG), substrate shrinkage (SS) and whole-domain compression (WDC) at substrate pre-stretches  $\lambda_{1s}^0 = 1$  and  $\lambda_{1s}^0 = 3$  are compared to the analytical solution in [27].

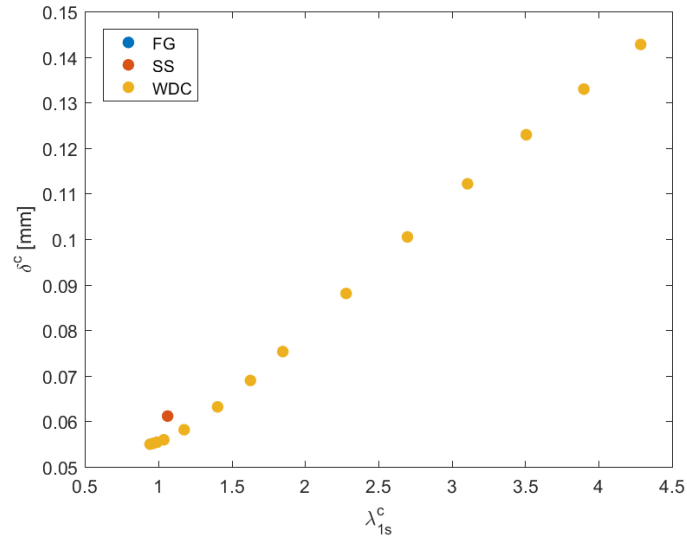
Figure 9 shows the sensitivity of the critical film compression  $\delta^c$  towards the critical film thickness  $t^c$ . The analytical solution predicts that the critical compression remains unaffected by the film thickness. However, for differential-growth-induced instabilities we observe a slight increase in  $\delta^c$  with increasing thickness  $t^c$ . We attribute this to the fact that the film thickness affects the deformation state in the substrate. As the simulation domain can expand freely in x-direction, the domain length at the instability point is determined by the equilibrium of forces between the compressed film and the stretched substrate. As thicker films behave stiffer, the substrate is stretched farther until an equilibrium is reached, which results in a larger critical substrate stretch  $\lambda_{1s}^c$ . This hypothesis is supported by the observation that the results for differential growth approach the analytical solution for  $t^c \rightarrow 0$ . For an infinitely thin film, it holds that  $\lambda_{1s}^c = 1$  as assumed in the analytical solution. For whole-domain compression, the substrate stretch is independent of the film thickness, and we indeed observe constant critical compressions  $\delta^c$ , denoted in yellow and green in Figure 9. Nevertheless, the magnitude increases with increasing substrate pre-stretch  $\lambda_{1s}^0$ . We note that the critical compression for the smallest film thickness  $t^0 = 0.15\text{mm}$  appears unexpectedly high compared to all other values. This might be an artifact of the finite element discretization: for the smallest film thickness we approach the limit of our mesh refinement as indicated in Section 3(g).

Figure 10 illustrates the critical film compression  $\delta^c$  as a function of the stiffness ratio  $\mu_f/\mu_s$ . For all origins of compression the critical film compression  $\delta^c$  decreases asymptotically with increasing stiffness ratio  $\mu_f/\mu_s$  in agreement with the analytical solution in Section 2 predicting  $\delta^c \sim (\mu_f/\mu_s)^{-2/3}$ . We observe that film growth and substrate shrinkage not only yield identical



**Figure 10.** Critical compression  $\delta^c$  as a function of the stiffness ratio  $\mu_f/\mu_s$  for film growth (FG), substrate shrinkage (SS) and whole-domain compression (WDC) at substrate pre-stretches  $\lambda_{1s}^0 = 1$  and  $\lambda_{1s}^0 = 3$ . The computational results are compared to the analytical solution in [27]. All results correspond to a critical film thickness of  $t^c = 0.35\text{mm}$ .

critical wavelengths  $\lambda^c$  but also identical critical film compressions  $\delta^c$ . Independent of the stiffness ratio  $\mu_f/\mu_s$ , increasing pre-stretch  $\lambda_{1s}^0$  results in higher critical film compressions  $\delta^c$ . To



**Figure 11.** Critical compression  $\delta^c$  as a function of the critical substrate stretch  $\lambda_{1s}^c$  for stiffness ratio  $\mu_f/\mu_s = 29$ . Film growth (FG) and substrate shrinkage (SS) yield identical results, while the critical compression increases almost linearly with the critical substrate stretch for whole-domain compression (WDC), depending on the substrate pre-stretch  $\lambda_{1s}^0$ .

further investigate these differences, Figure 11 plots the critical film compression  $\delta^c$  as a function

of the substrate stretch at the instability point  $\lambda_{1s}^c$ . Expectedly, the critical substrate stretch is identical for film growth and substrate shrinkage. For whole domain compression, however, we observe an almost linear relation between the critical film compression and the critical substrate stretch, dependent on the substrate pre-stretch  $\lambda_{1s}^0$ . In general, the critical compression appears slightly higher for film growth or substrate shrinkage than for whole domain compression at similar substrate stretch state.

### (b) Post-buckling evolution

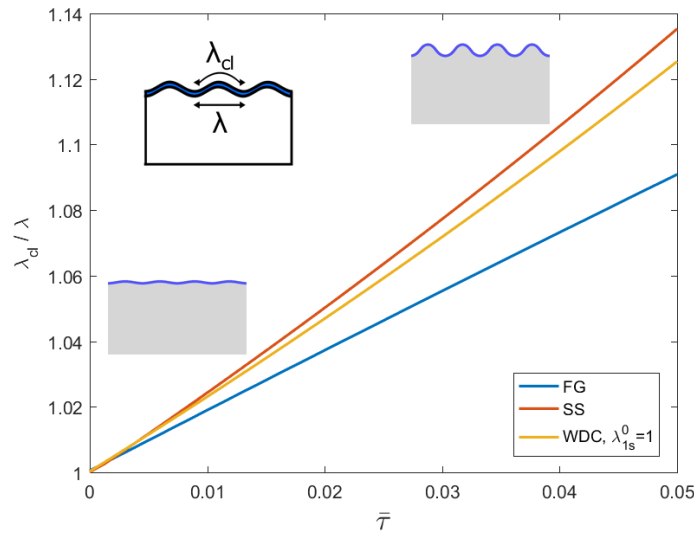


**Figure 12.** Post-critical evolution of the morphology ratio of curvilinear over Cartesian wavelength  $\lambda_{cl}/\lambda$  for film growth (FG), substrate shrinkage (SS) and whole-domain compression (WDC) without substrate pre-stretch. We denote the post-critical simulation pseudo-time as  $\bar{\tau} = \tau - \tau^c$ , with the critical time  $\tau^c$ . All results correspond to a critical film thickness of  $t^c = 0.35\text{mm}$  and a stiffness ratio of  $\mu_f/\mu_s = 29$ .

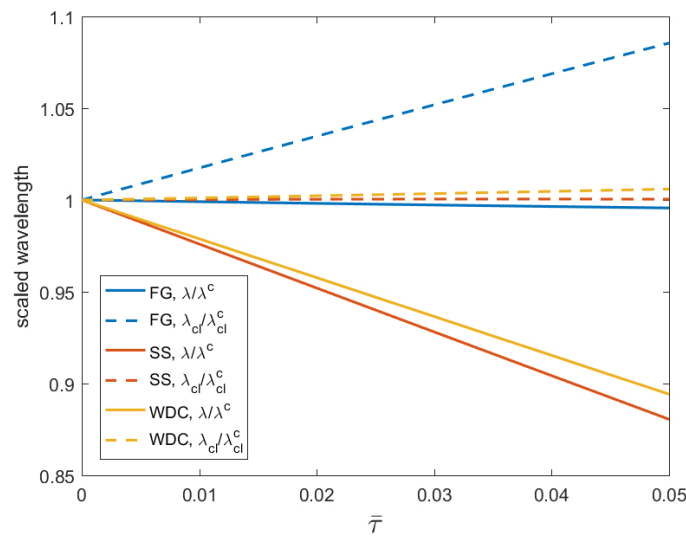
Evaluating both the curvilinear wavelength  $\lambda_{cl}$  and the Cartesian wavelength  $\lambda$  is a convenient method to characterize the post-buckling evolution of wrinkling patterns [20,21]. While the Cartesian wavelength is simply measured along the length of the bilayer, the curvilinear wavelength  $\lambda_{cl}$  is the corresponding wavelength along the surface of the wrinkled film (see Figure 12). At the instability point, a wrinkling pattern with infinitesimal amplitudes is established, so that  $\lambda_{cl}^c \approx \lambda^c$ . As compression increases, wrinkle amplitudes grow and the morphology ratio  $\lambda_{cl}/\lambda$  increases.

Figure 12 plots the morphology ratio  $\lambda_{cl}/\lambda$  against the simulation pseudo-time  $\tau$  for the post-critical domain. While whole-domain compression and substrate shrinkage exhibit a progressive increase in the morphology ratio  $\lambda_{cl}/\lambda$ , film growth results in a degressive curve. Although film growth and substrate shrinkage yield identical critical wavelengths and critical film compressions, this suggests a different post-buckling behavior.

Figure 13 plots  $\lambda_{cl}$  and  $\lambda$  separately for each origin of compression. In the case of whole-domain compression and substrate shrinkage, the curvilinear wavelength  $\lambda_{cl}$  remains constant, while the Cartesian wavelength  $\lambda$  decreases, which results in an accordion-like contraction of the wrinkles [21]. On the contrary, for film growth the Cartesian wavelength  $\lambda$  remains constant and the

curvilinear wavelength  $\lambda_{cl}$  increases. In other words, the wrinkles “grow” in amplitude, while the wavelength is conserved. Notably, while film growth and substrate shrinkage yield almost identical critical conditions at the instability point, those mechanisms differ significantly in their post-buckling evolution.

Based on these observations, we are able to estimate the critical wavelength  $\lambda^c$  of wrinkling patterns from their post-buckling configuration. For whole-domain compression or substrate shrinkage, it holds that the critical wavelength can be determined from the curvilinear wavelength of the post-critical configuration as  $\lambda^c \approx \lambda_{cl}$ . On the contrary, for film growth the critical wavelength can be determined from the Cartesian wavelength of the post-critical configuration as  $\lambda^c \approx \lambda$ .



**Figure 13.** Post-critical evolution of scaled curvilinear wavelength  $\lambda_{cl}/\lambda_{cl}^c$  and scaled Cartesian wavelength  $\lambda/\lambda^c$  for film growth (FG), substrate shrinkage (SS) and whole-domain compression (WDC) without substrate pre-stretch, where  $\lambda_{cl}^c \approx \lambda^c$ . We denote the post-critical simulation pseudo-time as  $\bar{\tau} = \tau - \tau^c$ , with the critical time  $\tau^c$ . All results correspond to a critical film thickness of  $t^c = 0.35\text{mm}$  and a stiffness ratio of  $\mu_f/\mu_s = 29$ .

### (c) Secondary instabilities

When a wrinkled bilayer as displayed in Figure 14(a) is further compressed, secondary or even tertiary instabilities might arise. Pattern selection for secondary instabilities proved sensitive to the stiffness ratio  $\mu_f/\mu_s$ , the substrate pre-stretch  $\lambda_{1s}^0$ , the film thickness  $t^0$  and also the origin of compression. Superimposing these factors non-trivially evokes either folding, mountain ridge mode or period-doubling as illustrated in Figures 14(b)–14(d). For the case of period-doubling, we even observed a tertiary period-quadrupling bifurcation when compression continued beyond the second instability point as shown in Figure 14(e).

In a first step, we assess the influence of the stiffness ratio  $\mu_f/\mu_s$  and the pre-stretch  $\lambda_{1s}^0$  on the secondary pattern selection using whole-domain compression and a modest film thickness of  $t^0 = 0.35\text{mm}$ . This setup ensures comparability with earlier studies such as [20–22]. Figure 15 illustrates the secondary instability patterns resulting from different combinations of the stiffness ratio  $\mu_f/\mu_s$  and the pre-stretch  $\lambda_{1s}^0$ . Folding only occurs for small ratios  $\mu_f/\mu_s$  and pre-stretches

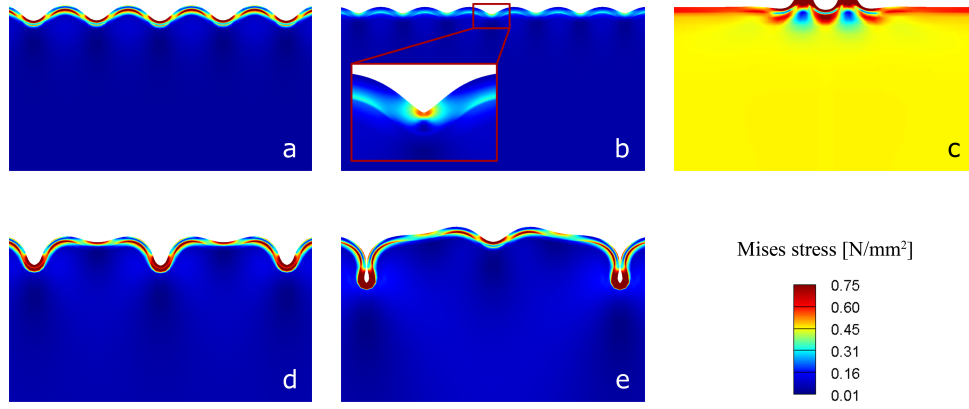


**Figure 14.** Primary, secondary and tertiary instability patterns observed in our numeric study: (a) primary wrinkling instability, (b) secondary cusped folding instability, (c) secondary mountain ridge instability, (d) secondary period-doubling instability, (e) tertiary period-quadrupling instability. The color map illustrates the von-Mises stress distribution.

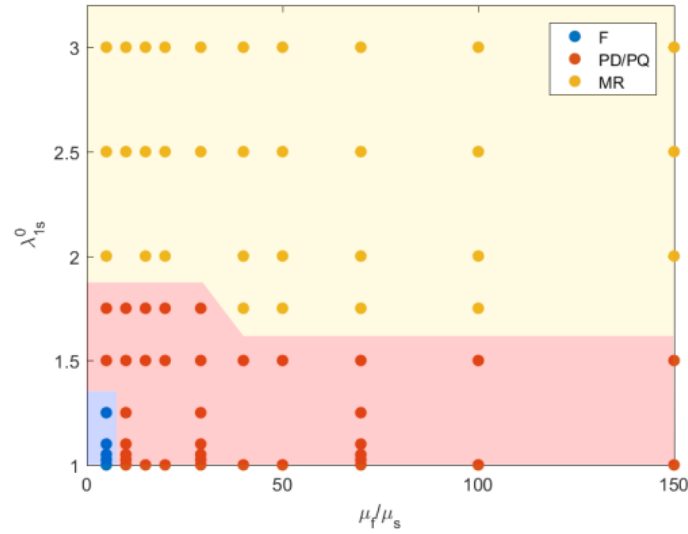


**Figure 15.** Pattern selection for secondary instabilities with respect to stiffness ratio  $\mu_f/\mu_s$  and substrate pre-stretch  $\lambda_{1s}^0$ . Depending on the stiffness ratio and substrate pre-stretch we observed either cusped folding (F), period-doubling which can eventually transition to period-quadrupling (PD/PQ) or mountain ridge mode (MR). All data was obtained with whole-domain compression and a modest film thickness of  $t^0 = 0.35\text{mm}$ .

$\lambda_{1s}^0$ . On the contrary, the mountain ridge mode requires large stiffness ratios  $\mu_f/\mu_s$  and/or pre-stretches  $\lambda_{1s}^0$ . For intermediate combinations, we observe period-doubling, which can later even transition to period-quadrupling.

In a second step, we assess the influence of the film thickness  $t^0$ . The mountain ridge mode only occurs for thicker films ( $t^0 > 0.3\text{mm}$ ). As the entire deformation concentrates in single ridges, the substrate experiences very large deformations under the ridge which requires a certain minimum film bending stiffness to prevent the film from collapsing into folds before ridges can form. The

bending stiffness is proportional to the film's Young's modulus and the cube of its thickness. Likewise, we do not observe folding for large film thicknesses  $t^0 > 0.35\text{mm}$ , as thick films behave too stiff to form cusped valleys.

Finally, we found that also the origin of compression controls secondary pattern selection. Generally, the mechanisms identified above for whole-domain compression are applicable to differential-growth-driven instabilities as well (also see [18,32]). However, we could not reproduce the mountain ridge mode with differential growth. We attribute this to the boundary conditions, which allow the domain to expand freely. For very stiff films, differential growth is primarily compensated for by increasing substrate stretch rather than film compression. Thus, it appears that we are unable to induce a sufficiently large film compression for the mountain ridge mode to appear.

## 5. Discussion

In this work, we have employed computational modeling to analyze the influence of the origin of compression on the critical conditions for wrinkling instabilities, as well as the post-buckling behavior with the emergence of secondary instability patterns. We have demonstrated that the well known *qualitative* dependencies for primary wrinkling instabilities  $\lambda^c \sim t^c$ ,  $\lambda^c \sim (\mu_f/\mu_s)^{1/3}$ ,  $\delta^c \sim (\mu_f/\mu_s)^{-2/3}$  hold regardless of the origin of compression. Our results agree with previous studies employing film growth [9], substrate shrinkage [18,19], and whole domain compression with and without pre-stretch individually [15,18,27,33]. Nevertheless, our systematic comparison shows that the critical wavelengths  $\lambda^c$  and critical film compressions  $\delta^c$  differ *quantitatively* for each origin of compression on otherwise identical setups. Our findings indicate that those differences can mostly be attributed to differences in the substrate stretch state. Hereby, larger critical substrate stretches  $\lambda_{1s}^c$  correspond to shorter critical wavelengths  $\lambda^c$  (see Figures 6-8) and larger critical compressions  $\delta^c$  (see Figures 9-11). The importance of the substrate stretch state at the onset of wrinkling for comparative evaluations of different origins of compression has previously been discussed through analytical consideration in [24]. The less advanced analytical solution adopted in the current work disagrees with the computational results for substrate pre-stretches  $\lambda_{1s}^0 > 1.5$  due to its limitation to small deformations (see Figure 8). While more advanced analytical approaches may yield more realistic results for large substrate stretches, their capability to predict the post-buckling evolution and occurrence of secondary instabilities remains limited [24].

Our systematic study confirms that film growth and substrate shrinkage yield identical critical substrate stretches  $\lambda_{1s}^c$  and consequently identical critical wavelengths  $\lambda^c$  and critical compressions  $\delta^c$  (see Figures 6-7, 9-10). It is tempting to speculate that any superposition of film growth and substrate shrinkage should yield identical results as well. This may offer new paths to simplify modeling of biological growth processes. However, our simulations demonstrate that the post-buckling evolution depends on the origin of compression. Wrinkling patterns evoked by film growth grow in amplitude but retain their wavelength  $\lambda$ . On the contrary, wrinkling patterns caused by substrate shrinkage and whole-domain compression exhibit an accordion-like behavior, where shrinking wavelengths compensate for growing amplitudes. In this case, the curvilinear wavelength  $\lambda_{cl}$  remains constant (see Figure 13). Provided that the origin of compression is known, it is possible to identify the critical wavelength  $\lambda^c$  from either the Cartesian or curvilinear wavelength of post-critical wrinkling patterns. For film growth it holds that  $\lambda^c \approx \lambda$ , while for whole-domain compression and substrate shrinkage  $\lambda^c \approx \lambda_{cl}$ .

We have shown that secondary pattern selection in the highly nonlinear post-buckling regime not only depends on the stiffness ratio  $\mu_f/\mu_s$ , substrate pre-stretch  $\lambda_{1s}^0$  and film thickness  $t^0$ , but also on the origin of compression. Folding is associated with small ratios  $\mu_f/\mu_s$  and pre-stretches  $\lambda_{1s}^0$ , the mountain ridge mode with large ratios  $\mu_f/\mu_s$  and/or pre-stretches  $\lambda_{1s}^0$  and period-doubling

with intermediate combinations (see Figure 15). These results agree well with previous studies investigating whole-domain compression with pre-stretch [20,22,33,36,37]. Although secondary instability patterns were predominantly determined by the stiffness ratio  $\mu_f/\mu_s$  and the substrate pre-stretch  $\lambda_{1s}^0$ , the film thickness  $t^0$  and the origin of compression have a strong regulatory influence: they can suppress certain patterns and favor others. In our numerical study, folding only occurred for reasonably thin films, while the mountain ridge mode only emerged for thicker films. We obtained similar results in polymer experiments previously published in [18]. Finally, differential growth suppressed the mountain ridge mode. To the authors' knowledge, previous examinations of the mountain ridge mode [22,33] have exclusively employed whole-domain compression. Our results indicate that current phase diagrams of secondary pattern selection [21] neglect important regulatory factors: the film thickness and origin of compression. Furthermore, our findings suggest that film compression and substrate pre-stretch need to be considered individually in phase diagrams. In [21], they are instead bundled in a generic quantity, denoted as mismatch stretch. This is reasonably accurate for large stiffness ratios and pre-stretches only. Recent results published in [38] further indicate that for systems with differentially growing layers, the ratio between film and substrate growth additionally contributes to pattern selection. Future studies are therefore required to generate comprehensive phase diagrams of secondary pattern selection that consider the great variety of regulatory factors.

We have gained fundamental understanding of how the origin of compression influences primary wrinkling patterns, the post-buckling evolution and secondary pattern selection by studying each origin separately. However, in real-life problems we generally experience temporally and/or spatially combined origins of compression. For example, growth rates and growth kinematics in biological growth processes can vary greatly over time, which leads to intricate multi-axial compression states. Similarly, the manufacturing of technical bilayers often involves heat treatment. Thus, mechanically induced whole-domain compression is coupled with thermally induced differential expansion. Our computational framework is designed to enable combined loadings, which will be subject of future investigations. It can easily be extended to two-dimensional origins of compression and arbitrary three-dimensional basis geometries. We are convinced that in the future similar computational models, which incorporate different origins of compression, can be successfully applied in the engineering of smart surfaces or the diagnosis of neuronal disorders.

## 6. Limitations

Our computational model provides new insights into geometrical instabilities in bilayers subject to different origins of compression, yet it has a number of limitations. Geometric instabilities often result in localized deformations, such as folding and creasing patterns, where almost the entire deformation is focused in cusped valleys. Here, an FEA-based setup as presented in the current work reaches its limits as localized instabilities require extremely dense meshes resulting in exceedingly long simulation run times. We are certain, that this limitation will be resolved eventually by the rapid advancement of computer hardware, which has already allowed computational models to progress from simple one-dimensional models [39] to complex three-dimensional models [10] in the last two decades.

Furthermore, we consciously refrained from implementing self-contact to maintain reasonable simulation run-times. Consequently, the evolution of instability patterns beyond the beginning of self-contact are out of the scope of the current investigations. Likewise, we assumed an infinitely strong adhesion between film and substrate and thus neglected effects like film delamination, which would have required, among other aspects, to introduce the adhesion energy as an additional quantity.

For the comparison of different origins of compression we chose a neo-Hookean material model



as the one most commonly used in simulations of geometric instabilities. However, constitutive modeling for soft and highly nonlinear materials proves very challenging [40,41]. Moreover, the neo-Hookean material model does not account for anisotropic or viscous material behavior. While we consider these limitations acceptable for our current parameter studies, the neo-Hookean material model is limited in its applicability to real-life problems.

## 7. Conclusion

In this work, we have presented a solid computational framework to evaluate the influence of the origin of film compression (film growth, substrate shrinkage, and whole domain compression with and without substrate pre-stretch) on geometric instabilities in bilayers. We have shown that the origin of compression controls the substrate stretch at the primary instability point, which – for nonlinear elastic materials – affects the stiffness ratio between film and substrate and thus the critical wavelength and critical compression. While film growth and substrate shrinkage yield identical critical conditions for primary wrinkling, they show a fundamentally different post-buckling behavior. Our results have further demonstrated that secondary instability patterns in the highly nonlinear post-buckling regime not only non-trivially depend on the stiffness ratio and the substrate pre-stretch but also on the film thickness and the origin of compression. Even for appropriate combinations of the stiffness ratio and substrate pre-stretch, folding necessitates thin films, while the mountain ridge mode only occurs for reasonably thick films and whole-domain compression. Future studies on secondary pattern selection should therefore expand existing phase diagrams by incorporating the roles of film thickness and origin of compression.

**Ethics.** The authors declare no misconducts of ethics.

**Data Accessibility.** This article has no additional data.

**Authors' Contributions.** S.A., P.S. and S.B. designed the research and discussed the outline, S.A. designed computational tools, performed simulations, and analyzed data. S.A. and S.B. drafted the paper. All authors discussed results and commented on the manuscript.

**Competing Interests.** The authors declare no competing interests.

**Funding.** This study was kindly supported by the German Research Foundation grant STE 544/50 and by the Cluster of Excellence Engineering of Advanced Materials (EAM) to P.S. and S.B.

**Acknowledgements.** P.S. acknowledges the Wolfson Award by The Royal Society.

## References

1. Yin J, Cao Z, Li C, Sheinman I, Chen X. 2008 Stress-driven buckling patterns in spheroidal core/shell structures. *Proceedings of the National Academy of Sciences of the United States of America* **105**, 19132–19135.
2. Yin J, Gerling GJ, Chen X. 2010 Mechanical modeling of a wrinkled fingertip immersed in water. *Acta biomaterialia* **6**, 1487–1496.
3. Asally M, Kittisopikul M, Rué P, Du Y, Hu Z, Çağatay T, Robinson AB, Lu H, Garcia-Ojalvo J, Süel GM. 2012 Localized cell death focuses mechanical forces during 3D patterning in a biofilm. *Proceedings of the National Academy of Sciences of the United States of America* **109**, 18891–18896.
4. Eskandari M, Pfaller M, Kuhl E. 2013 On the Role of Mechanics in Chronic Lung Disease. *Materials* **6**, 5639–5658.
5. Papastavrou A, Steinmann P, Kuhl E. 2013 On the mechanics of continua with boundary energies and growing surfaces. *Journal of the Mechanics and Physics of Solids* **61**, 1446–1463.
6. Richman DP, Stewart M, Hutchinson JW, Caviness, V. S. Jr.. 1975 Mechanical Model of Brain Convolutional Development. *Science* pp. 18–21.
7. Xu G, Knutsen AK, Dikranian K, Kroenke CD, Bayly PV, Taber LA. 2010 Axons pull on the brain, but tension does not drive cortical folding. *Journal of biomechanical engineering* **132**, 071013.

8. Ronan L, Voets N, Rua C, Alexander-Bloch A, Hough M, Mackay C, Crow TJ, James A, Giedd JN, Fletcher PC. 2014 Differential tangential expansion as a mechanism for cortical gyrification. *Cerebral cortex (New York, N.Y. : 1991)* **24**, 2219–2228.
9. Budday S, Steinmann P, Kuhl E. 2014 The role of mechanics during brain development. *Journal of the Mechanics and Physics of Solids* **72**, 75–92.
10. Tallinen T, Chung JY, Rousseau F, Girard N, Lefèvre J, Mahadevan L. 2016 On the growth and form of cortical convolutions. *Nature Physics* **12**, 588–593.
11. Hardan AY, Jou RJ, Keshavan MS, Varma R, Minshew NJ. 2004 Increased frontal cortical folding in autism: a preliminary MRI study. *Psychiatry research* **131**, 263–268.
12. Harris JM, Yates S, Miller P, Best, J. J. K., Johnstone EC, Lawrie SM. 2004 Gyrification in first-episode schizophrenia: a morphometric study. *Biological psychiatry* **55**, 141–147.
13. Khang DY, Rogers JA, Lee HH. 2009 Mechanical Buckling: Mechanics, Metrology, and Stretchable Electronics. *Advanced Functional Materials* **19**, 1526–1536.
14. Wagner S, Lacour SP, Jones J, Hsu PI, Sturm JC, Li T, Suo Z. 2004 Electronic skin: architecture and components. *Physica E: Low-dimensional Systems and Nanostructures* **25**, 326–334.
15. Stafford CM, Harrison C, Karim A, Amis EJ. 2002 Measuring the modulus of polymer films by strain-induced buckling instabilities. *Polymer Preprints* p. 1335.
16. Stafford CM, Harrison C, Beers K, Karim A, Amis EJ, VanLandingham MR, Kim HC, Volksen W, Miller RD, Simonyi EE. 2004 A buckling-based metrology for measuring the elastic moduli of polymeric thin films. *Nature materials* **3**, 545–550.
17. Piyadasa H, Altieri A, Basu S, Schwartz J, Halayko AJ, Mookherjee N. 2016 Biosignature for airway inflammation in a house dust mite-challenged murine model of allergic asthma. *Biology open* **5**, 112–121.
18. Budday S, Andres S, Walter B, Steinmann P, Kuhl E. 2017 Wrinkling instabilities in soft bilayered systems. *Philosophical transactions. Series A, Mathematical, physical, and engineering sciences* **375**.
19. Bowden N, Brittain S, Evans AG, Hutchinson JW, Whitesides GM. 1998 Spontaneous formation of ordered structures in thin films of metals supported on an elastomeric polymer. *Nature* **393**, 146–149.
20. Brau F, Vandeparre H, Sabbah A, Poulard C, Boudaoud A, Damman P. 2010 Multiple-length-scale elastic instability mimics parametric resonance of nonlinear oscillators. *Nature Physics* **7**, 56–60.
21. Wang Q, Zhao X. 2015 A three-dimensional phase diagram of growth-induced surface instabilities. *Scientific reports* **5**, 8887.
22. Cao Y, Hutchinson JW. 2012 Wrinkling Phenomena in Neo-Hookean Film/Substrate Bilayers. *Journal of Applied Mechanics* **79**, 031019.
23. Bigoni D, Bordignon N, Piccolroaz A, Stupkiewicz S. 2018 Bifurcation of elastic solids with sliding interfaces. *Proceedings. Mathematical, physical, and engineering sciences* **474**, 20170681.
24. Holland MA, Li B, Feng XQ, Kuhl E. 2017 Instabilities of soft films on compliant substrates. *Journal of the Mechanics and Physics of Solids* **98**, 350–365.
25. Biot MA. 1965 *Mechanics of Incremental Deformations*. New York: John Wiley & Sons, Inc.
26. Allen HG. 1969 *Analysis and design of structural sandwich panels*. The Commonwealth and international library. Structures and solid body mechanics division. Oxford and New York: Pergamon Press [1st ed.] edition.
27. Sun JY, Xia S, Moon MW, Oh KH, Kim KS. 2012 Folding wrinkles of a thin stiff layer on a soft substrate. *Proceedings of the Royal Society A: Mathematical, Physical and Engineering Sciences* **468**, 932–953.
28. Menzel A, Kuhl E. 2012 Frontiers in growth and remodeling. *Mechanics research communications* **42**, 1–14.
29. Bayly PV, Okamoto RJ, Xu G, Shi Y, Taber LA. 2013 A cortical folding model incorporating stress-dependent growth explains gyral wavelengths and stress patterns in the developing brain. *Physical biology* **10**, 016005.
30. Budday S, Raybaud C, Kuhl E. 2014 A mechanical model predicts morphological abnormalities in the developing human brain. *Scientific reports* **4**, 5644.
31. Javili A, Dortdivanlioglu B, Kuhl E, Linder C. 2015 Computational aspects of growth-induced instabilities through eigenvalue analysis. *Computational Mechanics* **56**, 405–420.
32. Budday S, Steinmann P, Kuhl E. 2015 Secondary instabilities modulate cortical complexity in the mammalian brain. *Philosophical magazine (Abingdon, England)* **95**, 3244–3256.

33. Liu J, Bertoldi K. 2015 Bloch wave approach for the analysis of sequential bifurcations in bilayer structures. *Proceedings of the Royal Society A: Mathematical, Physical and Engineering Science* **471**, 20150493.
34. Volynskii AL, Bazhenov S, Lebedeva OV, Bakeev NF. 2000 Mechanical buckling instability of thin coatings deposited on soft polymer substrates. *Journal of Materials Science* **35**, 547–554.
35. Toro R, Burnod Y. 2005 A morphogenetic model for the development of cortical convolutions. *Cerebral cortex (New York, N.Y. : 1991)* **15**, 1900–1913.
36. Zang J, Zhao X, Cao Y, Hutchinson JW. 2012 Localized ridge wrinkling of stiff films on compliant substrates. *Journal of the Mechanics and Physics of Solids* **60**, 1265–1279.
37. Zhuo L, Zhang Y. 2015 From period-doubling to folding in stiff film/soft substrate system: The role of substrate nonlinearity. *International Journal of Non-Linear Mechanics* **76**, 1–7.
38. Dortdivanlioglu B, Javili A, Linder C. 2017 Computational aspects of morphological instabilities using isogeometric analysis. *Computer Methods in Applied Mechanics and Engineering* **316**, 261–279.
39. Raghavan R, Lawton W, Ranjan SR, Viswanathan RR. 1997 A Continuum Mechanics-based Model for Cortical Growth. *Journal of Theoretical Biology* **187**, 285–296.
40. Martins, P. A. L. S., Natal Jorge, R. M., Ferreira, A. J. M.. 2006 A Comparative Study of Several Material Models for Prediction of Hyperelastic Properties: Application to Silicone-Rubber and Soft Tissues. *Strain* **42**, 135–147.
41. Budday S, Sommer G, Birkel C, Langkammer C, Haybaeck J, Kohnert J, Bauer M, Paulsen F, Steinmann P, Kuhl E, Holzapfel GA. 2017 Mechanical characterization of human brain tissue. *Acta biomaterialia* **48**, 319–340.